nature communications

Article

https://doi.org/10.1038/s41467-025-61836-5

Strategic energy-level modulation in porous heterojunctions: advancing gas sensing through Type-I to Type-II transitions

Received: 9 December 2024

Accepted: 2 July 2025

Published online: 18 July 2025

Check for updates

Yong-Jun Chen[1,2], Yi-Ming Xu[1,3], Xiao-Liang Ye[1,2], Zhi-Peng Luo[4], Shi-Peng Zhu[4], Ke-Feng Li[1], Jiang-Feng Lu[1], Guan-E Wang[1,2] & Gang Xu[1,2,5]

To significantly enhance reaction efficiency of porous heterojunctions in various applications, precise engineering of customization heterostructures through energy-level modulation is indispensable. Herein, the preparation of a core-shell porous heterojunction, UiO-66@TDCOF, is reported. Taking advantage of adjustable structure of metal-organic frameworks (MOFs), the energy-level of UiO-66 core is tailored to precisely align with that of porphyrin-based covalent organic framework (denoted as TDCOF) shell. As a results, the heterojunction transitions flexibly from a type-I to a type-II configuration, which remarkably enhances the efficiency of charge separation under light irradiation, resulting in exceptional performances in chemiresistive gas sensing. Notably, the sensitivity of $(NH_2)_{1.24}$-UiO-66@TDCOF towards NO_2 is at a high level among all reported heterojunctions under visible-light condition, surpassing the majority of previously reported MOF and COF materials. This research not only presents a strategy for the design of heterojunctions but also gives an approach to material design tailored for chemical applications.

The fabrication of heterojunctions represents an advanced approach in enhancing the performances of semiconductor materials[1–5]. This strategy is predicated on exceptional capability of heterojunction to efficiently dissociate charge carriers and to meticulously tailor the electronic and optical characteristics of the materials[6–10]. Heterojunctions formed from porous materials, such as metal-organic frameworks (MOFs)[11–13], covalent organic frameworks (COFs)[14–16], and hydrogen-bonded organic frameworks (HOFs)[17,18], are endowed with pore channels that facilitate facile access to the interface of heterojunction for chemical species (Fig. 1)[19]. This structural design not only effectively shields photogenerated electrons from being captured by impurities and defects during their diffusion process but also enhances their lifetime and mobility, thereby improving the efficiency of charge carrier separation.

To date, some works on the construction of heterojunctions with porous materials have reported inspiring results, highlighting the potential of porous heterojunctions materials in numerous chemical applications[20–25], including catalysis, energy conversion, and sensing. However, many applications necessitate the precise engineering of customization heterostructures through energy-level modulation to achieve energy-level alignment, thereby significantly enhancing reaction efficiency. The structure-adjustable MOFs and COFs offer a promising prospect to precisely regulate the energy-levels in porous heterojunction. This promotes the enhancement of performance improvement and the broadening of application for heterostructure materials.

Herein, a porous heterojunction is meticulously assembled by integrating UiO-66 and TDCOF, a pair of well-known typical MOF and

[1]State Key Laboratory of Structural Chemistry, Fujian Institute of Research on the Structure of Matter, Chinese Academy of Sciences (CAS) Fuzhou, Fujian 350002, PR China. [2]Fujian Science & Technology Innovation Laboratory for Optoelectronic Information of China, Fuzhou, Fujian 350108, PR China. [3]ShanghaiTech University, Shanghai 201210, PR China. [4]State Key Laboratory of Photocatalysis on Energy and Enviroment, College of Chemistry, Fuzhou University, Fuzhou, Fujian 350116, PR China. [5]University of Chinese Academy of Sciences (UCAS), Beijing 100049, PR China. e-mail: gxu@fjirsm.ac.cn

https://doi.org/10.1038/s41467-025-61836-5

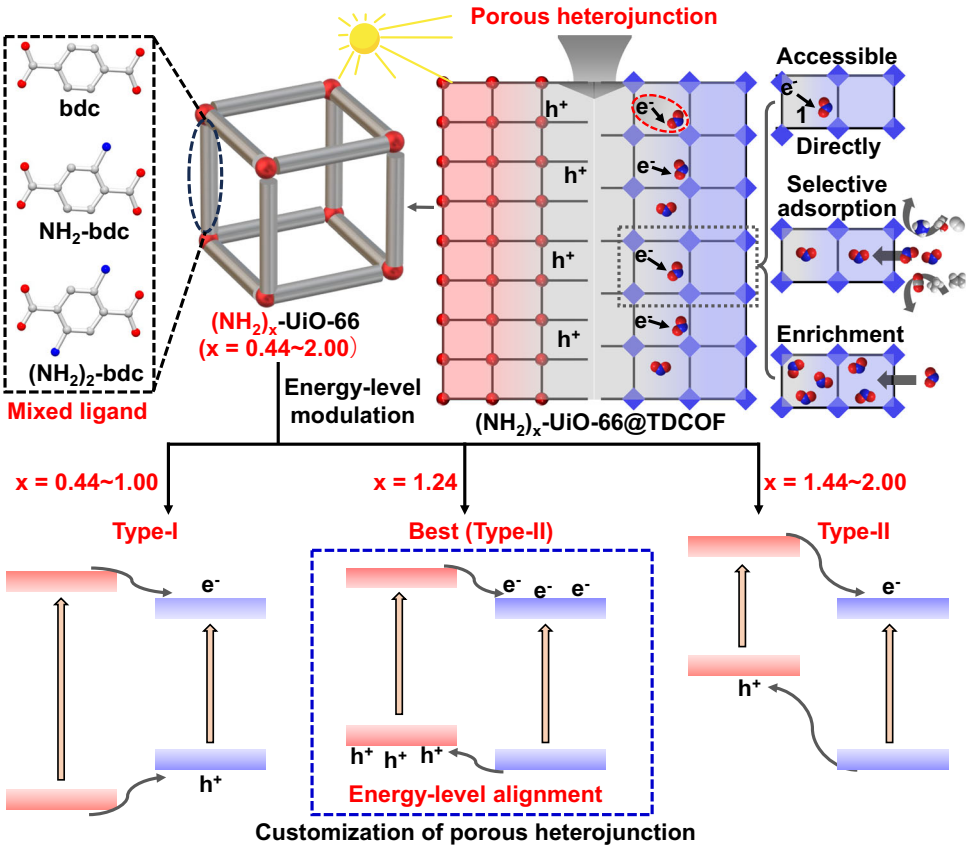

Fig. 1 | Schematic illustration of design protocol for the customization of porous heterojunction materials with superior reaction efficiency through energy-level modulation. Mixed ligand (O: red; N: blue; C: gray); x stands for the average amino amount in UiO-66; Type-I and Type-II denote different heterojunction types. By engineering ligands to synthesize UiO-66 with varying energy levels and combining them with TDCOF, different porous heterojunction can be constructed to enhance the reactivity.

COF materials. The resultant porous heterojunction material, with a core-shell structure, is denoted as UiO-66@TDCOF. To achieve the precise regulation of the energy-level within this heterojunction, the UiO-66 core is ingeniously modified by incorporating varying amounts of -NH_2 groups onto its bridging ligands (Fig. 1). The precise modulation of energy-level brings energy-level alignment between UiO-66 and TDCOF, enabling the customization of porous heterojunctions to achieve the transition from a Type-I to a Type-II configuration (Fig. 1). This transformation effectively enhances the efficiency of charge separation and modulating the chemical reactivity of the heterojunction. The advantages of selecting UiO-66 and TDCOF for the synthesis of core-shell structures are as follows: (1) UiO-66 possesses a stable framework that is amenable to functionalization, allowing for effective modification of COF materials and precise modulation of the energy-level[26]; (2) TDCOF has been identified as a material capable of providing active sites for gas sensing[27]; (3) The energy levels of UiO-66 and TDCOF exhibit good compatibility, facilitating the construction of heterojunctions. As a paradigmatic application that showcases the potential of the porous heterojunction, UiO-66@TDCOF was employed as a chemiresistive gas sensing material for NO_2. Through regulating the energy-level, the sensing performance of the porous heterojunction materials is optimized, underscoring the significance of meticulous engineering in crafting customization heterostructures to amplify their performance. Notably, the sensitivity of $(NH_2)_{1.24}$-UiO-66@TDCOF, the one with two -NH_2 in one bridging ligand to achieve the optimal heterostructure, toward NO_2 is at a high level in not only all known heterojunction materials under visible-light condition but also among all reported MOF and COF materials. Moreover, it demonstrates exceptional selectivity, a low detection limit, superior long-term stability, swift response, and recovery. The synergistic effects of UiO-66 and TDCOF is elucidated in the following aspects: (1) the construction of heterojunction bolsters the photoelectric separation efficiency; (2) the preserved porosity facilitates the enrichment and selective adsorption of the target gas; and (3) the amino group on the UiO-66 is pivotal for regulating the energy-level, while the imine bond on TDCOF serves as the specific functional motif for gas sensing. This work not only establishes a starting point for the exploration of MOF@COF hybrid materials in chemiresistive gas sensing applications, but also offers an avenue for the design of more advanced high-performance materials.

Results and Discussion

Structure Analysis and Characterizations

UiO-66 is precisely assembled from $Zr_6(OH)_4O_4$ cluster and 1,4-dicarboxybenzene ligands[26]. Through ligands design, a series of UiO-66 with different amount of amino dangling bonds, denoted as $(NH_2)_x$-UiO-66 (where x represents for average number of amino groups in single ligand ranging from 0.44 to 2.00), are synthesized under solvothermal conditions (further details can be found in the methods section). Powder X-ray diffraction (PXRD) shows that the phase of these $(NH_2)_x$-UiO-66 is consistent with simulated UiO-66 (Supplementary Fig. 3a). Subsequently, these $(NH_2)_x$-UiO-66 materials are introduced into the reaction system of TDCOF for in-situ synthesis of $(NH_2)_x$-UiO-66@TDCOF porous heterojunction materials. TDCOF is successfully synthesized from 5,10,15,20-tetrakis(4-aminophenyl)porphyrin (TAPP) and 2,6-diformylpyridine (DFP) through the Schiff base reactions under solvothermal conditions (Supplementary Fig. 3b)[27]. In the crystal structure of TDCOF, one TAPP molecule is connected with four DFP

https://doi.org/10.1038/s41467-025-61836-5

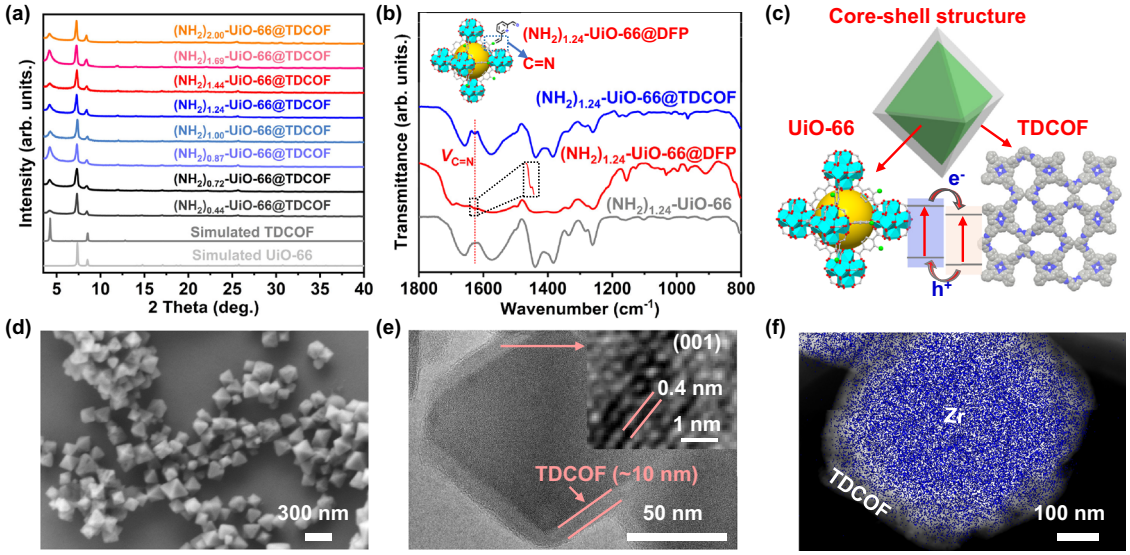

Fig. 2 | Characterizations of $(NH_2)_x$-UiO-66@TDCOF. a PXRD patterns of $(NH_2)_x$-UiO-66@TDCOF. **b** FT-IR spectra of $(NH_2)_{1.24}$-UiO-66, $(NH_2)_{1.24}$-UiO-66@DFP, and $(NH_2)_{1.24}$-UiO-66@TDCOF (The red line indicates the imine bond peak). **c** Core-shell structure model of UiO-66@TDCOF. **d** SEM image of $(NH_2)_{1.24}$-UiO-66@TDCOF. **e** HR-TEM image (inset: lattice fringe, d = 0.4 nm) of $(NH_2)_{1.24}$-UiO-66@TDCOF (TDCOF thickness = ~10 nm). **f** High-angle annular dark-field scanning TEM (HAADF-STEM) and elemental mapping analysis of $(NH_2)_{1.24}$-UiO-66@TDCOF. Each experiment was independently repeated three times to obtain similar results in Fig. 2d-f. Source data are provided as a Source Data file.

molecules while one DFP molecule is connected with two TAPP molecules to form 2D π-conjugated macromolecular layers in *ab* plane with layer spacing of 0.403 nm (Supplementary Fig. 4).

Through meticulously adjusting the preparation method of TDCOF, it is found that TDCOF could be effectively incorporated into a hybrid structure with $(NH_2)_x$-UiO-66, resulting in the formation of $(NH_2)_x$-UiO-66@TDCOF. Those are confirmed by PXRD patterns and Fourier transform infrared (FT-IR) spectra (Fig. 2a and Supplementary Fig. 5). The PXRD patterns reveal an intense peak at $2\theta = 4.26°$ attributed to TDCOF, as well as intense peaks at 7.34° and 8.46° assigned to $(NH_2)_x$-UiO-66 (Fig. 2a). The FT-IR spectra show a new peak near 1622 cm^{-1}, corresponding to the characteristic vibration of the C = N bond, indicating the presence of imine linkages within $(NH_2)_x$-UiO-66@TDCOF (Supplementary Fig. 5). These results collectively demonstrate that the structures of $(NH_2)_x$-UiO-66@TDCOF are consistent with $(NH_2)_x$-UiO-66 and TDCOF. Furthermore, a new peak corresponding to imine bond is also observed in the FT-IR spectrum of $(NH_2)_{1.24}$-UiO-66@DFP, suggesting that $(NH_2)_{1.24}$-UiO-66 and DFP could form covalent bonds in the interface (Fig. 2b and Supplementary Fig. 6). The preparation conditions of $(NH_2)_{1.24}$-UiO-66@DFP are similar to those for $(NH_2)_x$-UiO-66@TDCOF except that TAPP is not added to the reaction system. As a monomer for the synthesis of TDCOF, DFP also needs to be added in the preparation of $(NH_2)_x$-UiO-66@TDCOF. Within the preparation system of $(NH_2)_x$-UiO-66@TDCOF, DFP can not only form imine bonds with TAPP on the TDCOF framework but also form imine bonds with the amino groups of $(NH_2)_x$-UiO-66 at the interface. These finding collectively implies covalent-bonded connection between $(NH_2)_x$-UiO-66 and TDCOF within $(NH_2)_x$-UiO-66@TDCOF.

Scanning electron microscopy (SEM) and transmission electron microscopy (TEM) tests were carried out to investigate the morphology of the samples. For $(NH_2)_x$-UiO-66, all samples exhibit regular octahedral shapes with particle sizes ranging from 50 to 300 nm in SEM images (Supplementary Figs. 7-14). Upon coating with TDCOF, $(NH_2)_x$-UiO-66@TDCOF all maintain their octahedral morphology, but the surface appears rougher when compared to pristine $(NH_2)_x$-UiO-66 (Fig. 2c, d and Supplementary Figs. 7-14). TEM images reveal the core-shell structure for the $(NH_2)_x$-UiO-66@TDCOF samples (Fig. 2c and Supplementary Figs. 11b and 15-16). Taking examples for $(NH_2)_{1.24}$-UiO-66@TDCOF, high resolution TEM (HR-TEM) shows a clear core-shell interface with shell thickness of ~10 nm and the shell material with a lattice fringe is close to the layer distance of TDCOF (001, d = 0.4 nm) (Fig. 2e). Furthermore, high-angle annular dark-field scanning TEM (HAADF-STEM) and element mapping images confirm the core-shell structure in $(NH_2)_{1.24}$-UiO-66@TDCOF, where the Zr element is densely distributed within the UiO-66 core (Fig. 2f). These results indicate successful and uniform coating of TDCOF layer on the surface of $(NH_2)_x$-UiO-66 to form core-shell octahedral structure.

N_2 adsorption tests were conducted at 77 K on $(NH_2)_{1.24}$-UiO-66, TDCOF, and $(NH_2)_{1.24}$-UiO-66@TDCOF to evaluate their porosity. Before that, the thermal stability tests were conducted to reveal an activation temperature of 200 °C for these samples (Supplementary Figs. 17-18). $(NH_2)_{1.24}$-UiO-66@TDCOF exhibits a specific surface area (S_{BET}) of 943 $m^2 g^{-1}$ with the pore size distribution fitted at 0.7, 1.2, and 1.3 nm, which corresponds to the pore sizes in the crystal structure of UiO-66 (0.7 and 1.3 nm) and simulated structure of TDCOF (1.2 nm), respectively (Supplementary Fig. 19). The S_{BET} of $(NH_2)_{1.24}$-UiO-66@TDCOF, while slightly lower than that of $(NH_2)_{1.24}$-UiO-66 (1140 $m^2 g^{-1}$), surpasses that of TDCOF (845 $m^2 g^{-1}$) (Supplementary Fig. 19). This result demonstrates that the S_{BET} and porosity of $(NH_2)_x$-UiO-66@TDCOF are retained. Notably, the S_{BET} of MOF or COF composite with other materials is typically reduced[28,29]. The retention of S_{BET} is a prominent advantage of the porous heterojunction materials, which would be beneficial for various chemical applications.

The energy-level structures of $(NH_2)_x$-UiO-66 and TDCOF are determined through UV-Vis absorption spectra and Mott-Schottky (MS) measurements[30,31]. As shown in Fig. 3a and Supplementary Figs. 20-27, as the number of amino dangling bonds increased in $(NH_2)_x$-UiO-66, the valence band (VB) continuously increases from -6.74 to -5.43 eV and the conduction band (CB) increases from -3.86 to -2.99 eV. The VB/CB positions of TDCOF are revealed to be -6.07 eV/-4.48 eV (Supplementary Fig. 28). These results show the energy-level relationships between $(NH_2)_x$ -UiO-66 and TDCOF changes from a straddled gap (x from 0.44 to 1.00) to a staggered gap (x from 1.24 to 2.00) (Fig. 3a).

https://doi.org/10.1038/s41467-025-61836-5

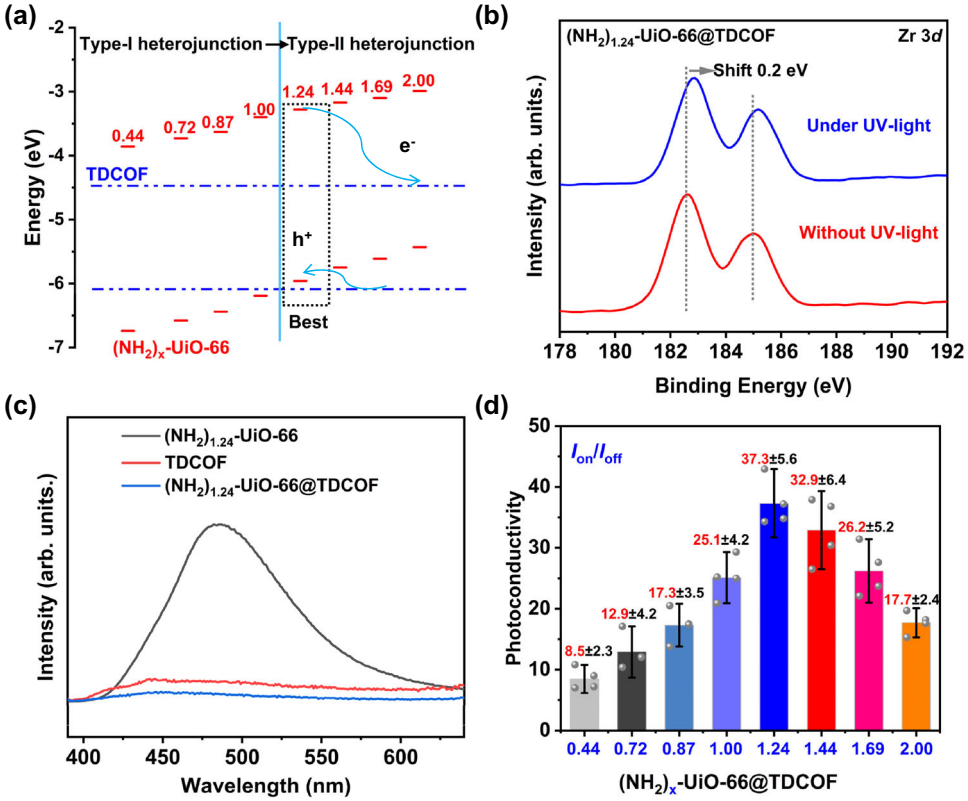

Fig. 3 | Band structure of (NH2)x-UiO-66@TDCOF. a Charge-transfer process under light irradiation based on the heterojunction. **b** In-situ XPS for Zr 3*d* under the dark and light irradiation for $(NH_2)_{1.24}$-UiO-66@TDCOF. **c** Photoluminescence measurements of $(NH_2)_x$-UiO-66, TDCOF, and $(NH_2)_{1.24}$-UiO-66@TDCOF. **d** Photoconductivity measurements of $(NH_2)_x$-UiO-66@TDCOF (x from 0.44 to 2.00, the error bar represents the maximum deviation between five data sets and their corresponding average). Source data are provided as a Source Data file.

To determine the type of the heterojunctions, $(NH_2)_x$-UiO-66@TDCOF (x from 1.00 to 1.44) were measured by in-situ X-ray photoelectron spectroscopy (XPS). As shown in XPS full spectra of $(NH_2)_{1.24}$-UiO-66@TDCOF, the structure of $(NH_2)_{1.24}$-UiO-66@TDCOF exhibits no discernible alteration under photic exposure relative to its pre-irradiation state (Supplementary Fig. 29). The FT-IR spectra show that the structure of $(NH_2)_{1.24}$-UiO-66@TDCOF remains basically unchanged after illumination (Supplementary Fig. 30). The high-resolution XPS spectra show that Zr 3*d* peak of $(NH_2)_x$-UiO-66@TDCOF (x from 1.00 to 1.44) shifts 0.13, 0.2, and 0.15 eV towards higher binding energy under light irradiation, respectively, indicating a decrease in electron density around Zr (Fig. 3b and Supplementary Fig. 31)[32]. However, pure $(NH_2)_{1.24}$-UiO-66 exhibits that peak of Zr 3*d* shifts 0.16 eV towards lower binding energy, indicating an increase in electron density around Zr (Supplementary Fig. 32). These results indicate that photogenerated electrons are transferred from $(NH_2)_x$-UiO-66 to TDCOF in porous heterojunction materials. Combination with the energy-level structure and the electron-transfer path, it is demonstrated that a straddled gap forms a type-I heterojunction, while a staggered gap forms a type-II heterojunction (Fig. 3a). Through precise energy-level modulation, the heterojunction in $(NH_2)_x$-UiO-66@TDCOF achieves transition from type-I to type-II at x = 1.24 (Fig. 3a). Photoluminescence (PL) measurements using $(NH_2)_{1.24}$-UiO-66@TDCOF as an example shows weaker intensity compared to that of $(NH_2)_{1.24}$-UiO-66 and TDCOF (Fig. 3c). Meanwhile, all $(NH_2)_x$-UiO-66@TDCOF samples exhibited higher photoconduction response than $(NH_2)_x$-UiO-66 and TDCOF under visible-light (Fig. 3d and Supplementary Fig. 33). These results clearly indicated the successful fabrication of the heterojunction structure and they can effectively enhance electron-hole pair separation.

Among these porous heterojunction materials, the most pronounced photoconduction response is observed in $(NH_2)_{1.24}$-UiO-66@TDCOF (Fig. 3d). The superior performance could be attributed to two main factors. Firstly, compared with the type-I heterojunction, type-II heterojunction could achieve effective interface transfer and spatial separation of electrons and holes under photoexcitation condition, thereby achieving higher charge separation efficiency (Fig. 3a)[33]. Secondly, the increase of the energy-level difference between two semiconductors, specifically from $(NH_2)_{1.24}$-UiO-66@TDCOF to $(NH_2)_{2.00}$-UiO-66@TDCOF, results in a higher barrier for charge transfer at heterogeneous interfaces (Fig. 3a)[34]. This increased barrier would impede charge transfer, leading to a decreased efficiency in charge separation when moving from $(NH_2)_{1.24}$-UiO-66@TDCOF to $(NH_2)_{2.00}$-UiO-66@TDCOF. Consequently, $(NH_2)_{1.24}$-UiO-66@TDCOF, featuring a type-II heterojunction and an optimally matched energy-level, stand out with the highest photoconductive response among these porous heterojunction materials.

Gas Sensing Measurements

$(NH_2)_x$-UiO-66@TDCOF porous heterojunction possesses high porosity and excellent photoactivity, thus might serve as desired platforms in chemistry applications. As an example, the chemiresistive gas sensing of $(NH_2)_x$-UiO-66@TDCOF is tested at room temperature and visible-light conditions using a home-made system[35]. Under visible-light and room temperature conditions, the test devices show the baseline current (~1 pA) that could be monitored by the instrument (Supplementary Fig. 34). All $(NH_2)_x$-UiO-66@TDCOF exhibit a pronounced increase in current in response to 100 ppm NO_2 (Fig. 4a and Supplementary Fig. 35-41). The response values display in a volcano-shape trend when x change from 0.44 to 2.00 (Fig. 4b). The response reaches up to a maximum value of 6046 at x = 1.24 (Fig. 4b).

https://doi.org/10.1038/s41467-025-61836-5

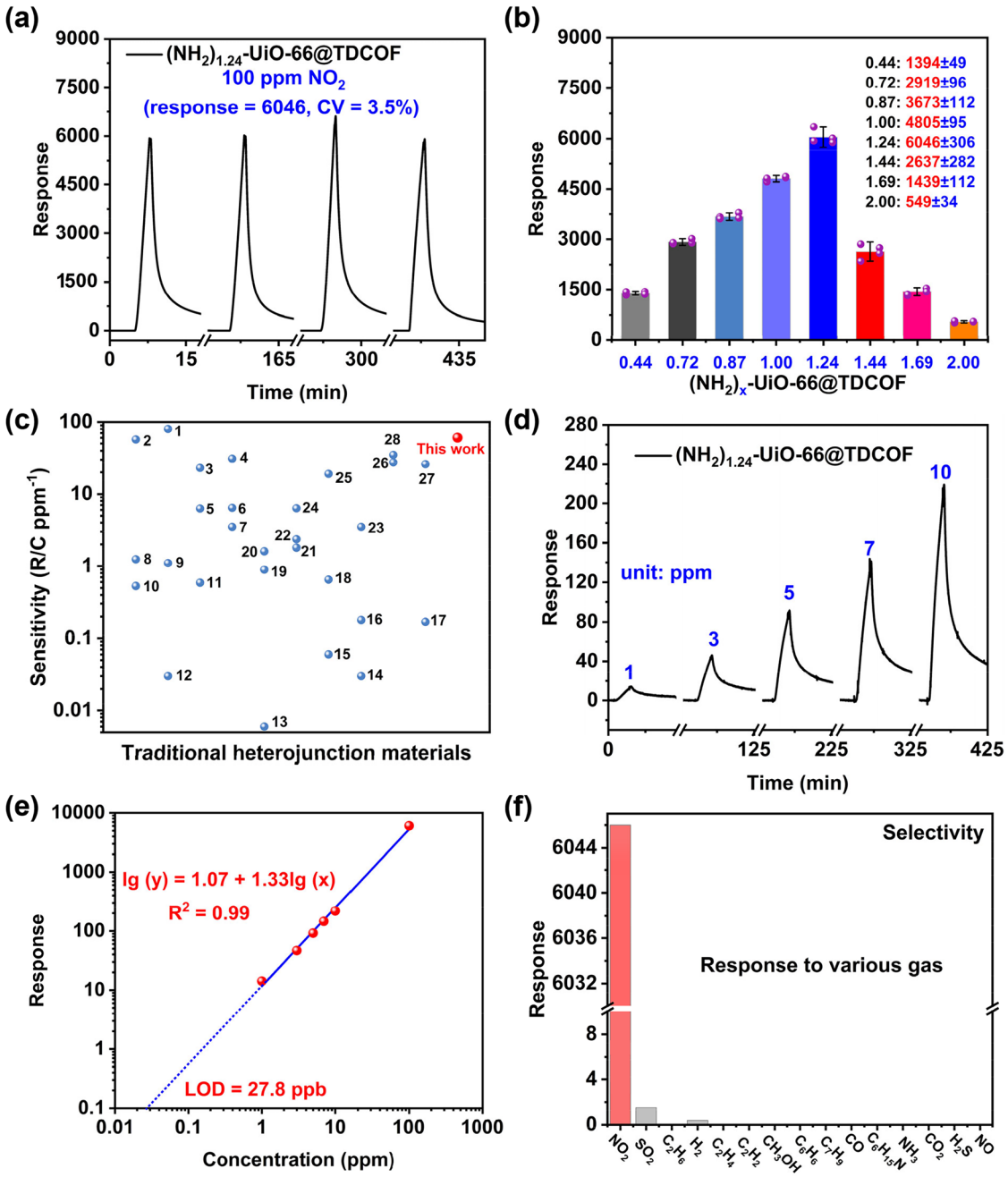

Fig. 4 | Gas sensing performances of (NH2)x-UiO-66@TDCOF under visible-light and room temperature. a Recycle sensing of $(NH_2)_{1.24}$-UiO-66@TDCOF towards 100 ppm NO_2. **b** Column chart of responses toward 100 ppm NO_2 of $(NH_2)_x$-UiO-66@TDCOF (x from 0.44 to 2.00, the error bar represents the maximum deviation between five data sets and their corresponding average). **c** Performance comparison to between $(NH_2)_{1.24}$-UiO-66@TDCOF and traditional heterojunction sensing materials (The number corresponding to the materials name in Supplementary Table 7). **d** Response-recovery curve towards NO_2 with different concentration for $(NH_2)_{1.24}$-UiO-66@TDCOF (All minor ticks are the same and value is 12.5). **e** Response-concentration log-log plots for $(NH_2)_{1.24}$-UiO-66@TDCOF (LOD = 27.8 ppb). **f** Gas sensing responses of $(NH_2)_{1.24}$-UiO-66@TDCOF to various gases. Source data are provided as a Source Data file.

Remarkably, the sensitivity (ratio of response value to concentration (R/C, ppm^{-1})) of $(NH_2)_{1.24}$-UiO-66@TDCOF toward NO_2 is at a high level among all reported heterojunction material under visible-light and room temperature conditions (Fig. 4c and Supplementary Table 4)[36–46] surpassing the majority of previously reported MOF and COF materials (Supplementary Table 5)[47–51].

$(NH_2)_{1.24}$-UiO-66@TDCOF also shows concentration-dependent response to NO_2 within the range of 1 to 100 ppm (Fig. 4d). The theoretical limit of detection (LOD) is calculated to be approximately 27.8 ppb, derived from the simulated linear equation by setting the response at 10% (Fig. 4e). Furthermore, by normalizing the response-recovery curve of $(NH_2)_{1.24}$-UiO-66@TDCOF for 100 ppm NO_2, the response and recovery times of $(NH_2)_{1.24}$-UiO-66@TDCOF are estimated to be 2.54 and 7.58 min, respectively (Supplementary Fig. 42). The rapid response/recovery are attributed to the excellent adsorption/desorption behaviors of $(NH_2)_{1.24}$-UiO-66@TDCOF to 100 ppm NO_2 (Supplementary Fig. 43).

Selectivity is a vital parameter for the function evaluation of sensing materials[52]. $(NH_2)_{1.24}$-UiO-66@TDCOF was conducted to exposure in 15 types of common interfering gases. Apart from a minimal response to SO_2 and H_2, $(NH_2)_{1.24}$-UiO-66@TDCOF almost has no response to other interfering gases such as NO, CO, NH_3, H_2S,

https://doi.org/10.1038/s41467-025-61836-5

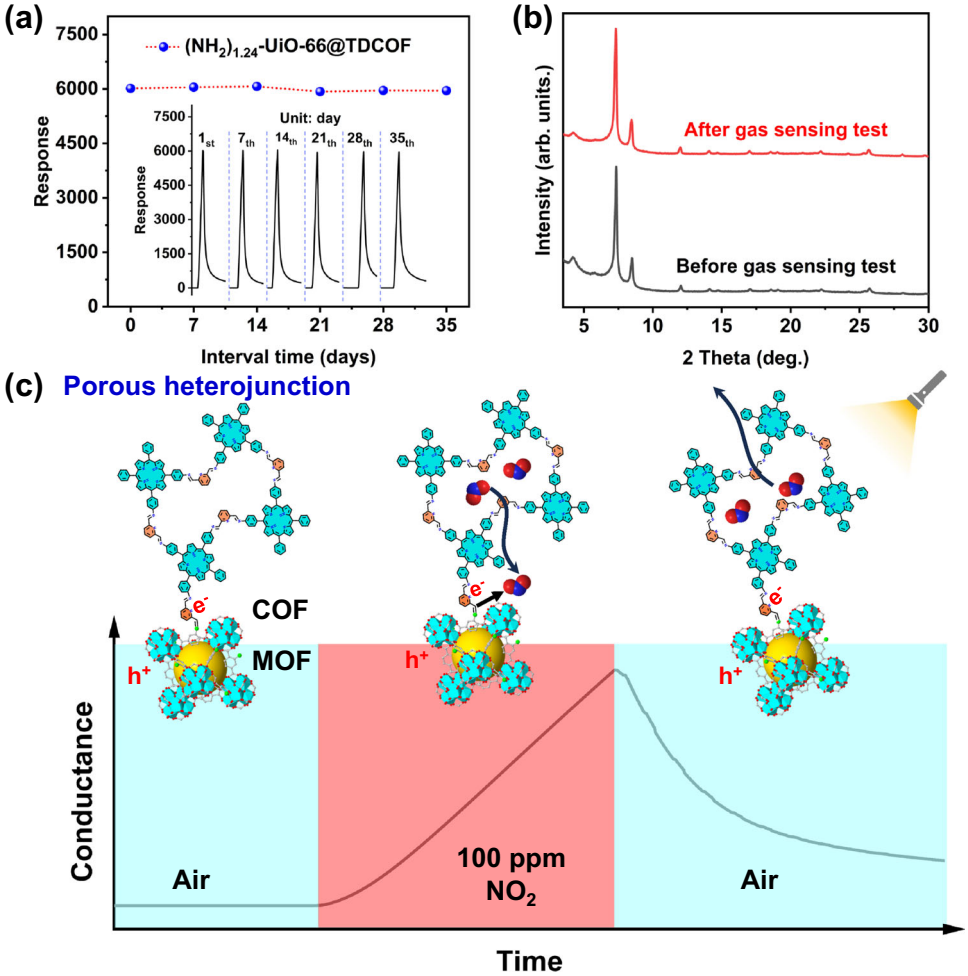

Fig. 5 | Sensing performances stability and sensing mechanism of (NH2)1.24-UiO-66@TDCOF. a Long-term stability of $(NH_2)_{1.24}$-UiO-66@TDCOF (inset: response-recovery curves toward 100 ppm NO_2 based on a seven-day interval). **b** PXRD patterns of $(NH_2)_{1.24}$-UiO-66@TDCOF before and after sensing test. **c** Possible sensing mechanism for $(NH_2)_{1.24}$-UiO-66@TDCOF. Under light, $(NH_2)_{1.24}$-UiO-66@TDCOF generates a significant number of photogenerated electrons via the heterojunction. These electrons are transferred to NO_2 adsorbed through the imine bond, thereby enhancing electrical conductivity. Source data are provided as a Source Data file.

and nitrobenzene (Fig. 4f and Supplementary Figs. 44-45). In addition, the response of $(NH_2)_{1.24}$-UiO-66@TDCOF to multi-gas environment containing NO_2, C_2H_4, C_2H_5OH, CO_2, and N_2O was evaluated using a static method. In the test system, the concentration of each gas is 1 ppm. The response to NO_2 in multi-gas environment closely resembles that observed for bare 1 ppm NO_2 (Supplementary Fig. 46). These results imply that $(NH_2)_x$-UiO-66@TDCOF exhibits excellent selectivity.

$(NH_2)_x$-UiO-66@TDCOF demonstrate the ability to be reused repeatedly in response to 100 ppm NO_2, with a coefficient of variation (CV) of less than 10% over four cycles (Fig. 4a and Supplementary Fig. 35-41). Meanwhile, after 35 days, it retains approximately 90% of its original response value to 100 ppm NO_2 (Fig. 5a). The structure integrity of $(NH_2)_{1.24}$-UiO-66@TDCOF remain intact after prolonged stability experiments, as confirmed by PXRD pattern (Fig. 5b). The morphology of $(NH_2)_{1.24}$-UiO-66@TDCOF remains unchanged before and after gas sensing test, as demonstrated by SEM tests (Supplementary Fig. 47). Above results indicate the porous heterojunction material has excellent repeatability and long-term stability. Overall, the materials designed with porous heterojunction strategy exhibits a relatively high level of comprehensive sensing performance as compared with other approaches (Supplementary Table 6).

Mechanism Studies

The sensing mechanism of $(NH_2)_{1.24}$-UiO-66@TDCOF is systematically investigated. Firstly, a series of control experiments have been conducted. $(NH_2)_{1.24}$-UiO-66 has no response to 100 ppm NO_2. TDCOF has a response value of 216 to 100 ppm NO_2, while 28.0 times lower than that of $(NH_2)_{1.24}$-UiO-66@TDCOF (Supplementary Fig. 48). The discrete TAPP molecules are coated on the surface of the $(NH_2)_{1.24}$-UiO-66 to obtain the comparative sample, denoted as $(NH_2)_{1.24}$-UiO-66/TAPP. The preparation conditions of $(NH_2)_{1.24}$-UiO-66/TAPP are similar to those for $(NH_2)_x$-UiO-66@TDCOF expect that DFP is not added to the reaction system. After coating TAPP, the color of sample changes from light yellow to black, indicating that TAPP molecules are successfully coated on $(NH_2)_{1.24}$-UiO-66 (Supplementary Fig. 49). This coating is based on the hydrogen bonding interactions between the amino functional groups of $(NH_2)_{1.24}$-UiO-66 and TAPP. SEM image shows that $(NH_2)_{1.24}$-UiO-66/TAPP has a similar morphology to $(NH_2)_x$-UiO-66@TDCOF (Fig. 2d and Supplementary Fig. 50). To illustrate the significance of porous COF layer on the NH_2-UiO-66 core, the response to 100 ppm NO_2 of $(NH_2)_{1.24}$-UiO-66/TAPP was conducted. The results indicate that $(NH_2)_{1.24}$-UiO-66@TDCOF has a response value that is 35 times higher than $(NH_2)_{1.24}$-UiO-66/TAPP (Fig. 4a and Supplementary Fig. 51). In addition, $(NH_2)_{1.24}$-UiO-66/TDCOF-50%, a physical mixture of $(NH_2)_{1.24}$-UiO-66 and TDCOF with the MOF loading of 50% has no response to light and 100 ppm NO_2

(Supplementary Figs. 48b and 52). These results suggest that the porous heterojunction structure effectively promotes the gas sensing performance of $(NH_2)_{1.24}$-UiO-66@TDCOF. Meanwhile, it is found that the response value to NO_2 under visible-light was 200 times higher than that under dark condition (Fig. 4a and Supplementary Fig. 53), suggesting light plays an important role in improving the sensing performance.

To further elucidate the significance of porous heterojunction in enhancing gas sensing, the photoconductivity and sensing tests were conducted under varying light conditions. The $(NH_2)_{1.24}$-UiO-66@TDCOF demonstrates a remarkable increase in photoconductivity and NO_2 sensing performance as the illumination transitioned from red to green and subsequently to blue light (Supplementary Fig. 54-55). As shown in Supplementary Fig. 56, the light absorption of $(NH_2)_{1.24}$-UiO-66 also exhibits a gradual enhancement from red to green and then to blue light, while the light absorption of TDCOF remains relatively unchanged. The result suggests that light absorption significantly influences the electron transition in $(NH_2)_{1.24}$-UiO-66, thereby affecting the quantity of photogenerated electrons transferred from $(NH_2)_{1.24}$-UiO-66 to TDCOF through the heterojunction. Consequently, within $(NH_2)_{1.24}$-UiO-66@TDCOF system, the light enhances gas sensing performance by boosting the charge separation efficiency at heterojunctions.

XPS and FT-IR measurements further reveal that specific functional motif in porous heterojunction for gas sensing. After $(NH_2)_{1.24}$-UiO-66@TDCOF was treated with 100 ppm NO_2 mixed air for 2 h, a new peak belonging to NO_2^- could be found in FT-IR (1381 cm^{-1}) and N 1 s XPS (405.8 eV) spectra to prove the adsorption of $(NH_2)_{1.24}$-UiO-66@TDCOF to NO_2 (Supplementary Figs. 57-58)[15,53,54]. Additionally, the C 1 s spectra reveal a peak at 285.9 eV (corresponding to C = N), which disappear and is replaced by a peak at 286.3 eV (corresponding to C-N) after NO_2 treatment (Supplementary Fig. 58)[15]. The N 1 s spectra reveal a peak at 398.2 eV (corresponding to C = N), which also disappear after NO_2 treatment (Supplementary Fig. 58)[15]. These results demonstrate that imine bond of TDCOF serves as specific functional motif for gas sensing performance.

The imine bond as sensing functional motif has the ability to adsorb acidic gases such as NO_2, SO_2, CO_2, and H_2S[55]. Through precisely engineering the energy-level structure, the integration of MOF and COF forms outstanding porous heterojunction. Under light, the porous heterojunction facilitates the efficient interfacial separation of electrons and holes, thereby bringing more photogenerated electrons. These photogenerated electrons accumulate on the imine bonds of TDCOF, conferring the materials with strong reducibility, which provides an excellent response to the highly oxidizing NO_2. In contrast, the oxidation capacities of CO_2 and H_2S are insufficient to elicit a significant response from $(NH_2)_x$-UiO-66@TDCOF (Fig. 4f). Therefore, the excellent NO_2 sensing selectivity of $(NH_2)_x$-UiO-66@TDCOF is attributed to the strong adsorption capacity of imine bonds for the highly oxidizing gas NO_2. In addition, exposure of $(NH_2)_{1.24}$-UiO-66@TDCOF to high purity N_2 resulted in negligible change in current (Supplementary Fig. 59). Moreover, the response of $(NH_2)_{1.24}$-UiO-66@TDCOF to 10 ppm NO_2 is comparable to that observed with N_2 and air as dilution gas (Supplementary Figs. 60-61). The result suggests that N_2 has little effect on NO_2 sensing. To perform a more comprehensive analysis of the selectivity mechanism, the adsorption energy ($E_{ad.}$) of imine bonds in $(NH_2)_x$-UiO-66@TDCOF for various gases has been calculated (Supplementary Fig. 62). In comparison to H_2, CO, CO_2, and other gases, the imine bond exhibits the highest adsorption energy (-0.44 eV) for NO_2, which further proves the highly selective response of $(NH_2)_x$-UiO-66@TDCOF towards NO_2 (Supplementary Fig. 63).

Based on above results, a possible sensing mechanism of $(NH_2)_{1.24}$-UiO-66@TDCOF porous heterojunction materials is proposed (Fig. 5c): 1) The XPS spectra after NO_2 treatment indicate that the imine bond in TDCOF can help to adsorb NO_2 (Supplementary Fig. 58). Upon exposure to NO_2, the $(NH_2)_{1.24}$-UiO-66@TDCOF with high porosity could effectively enrich the NO_2 (Supplementary Fig. 19); 2) The photoconductivity, photoluminescence, and in-situ XPS tests show that $(NH_2)_{1.24}$-UiO-66@TDCOF has improved charge separation efficiency (Fig. 3b-d). The dependence of light wavelength and comparison experiments indicate that the light absorption significantly influences sensing performance (Supplementary Figs. 54-56). In porous heterojunction materials, it is essential to utilize heterojunctions to generate a large number of photogenerated electrons, thereby enhancing gas sensing performance (Fig. 4b). 3) The photogenerated electrons are enriched on the imine bonds of TDCOF. The FT-IR and XPS spectra after NO_2 treatment demonstrate that NO_2 adsorbed on the imine bonds is converted to NO_2^- (Supplementary Figs. 57-58). Consequently, the photogenerated electrons were transferred from imine bond to NO_2 to form NO_2^- increasing the number of holes and enhancing conductivity; and 4) When exposed to bare air, NO_2^- was removed as it is oxidized by photogenerated hole[46], (Eq. (1)):

$$NO_2^- + h^+ \rightarrow NO_2 \quad (1)$$

releasing electrons and restoring conductivity. Overall, pure $(NH_2)_{1.24}$-UiO-66 exhibits negligible NO_2 sensing capabilities, while TDCOF shows a measurable NO_2 sensing ability (Supplementary Fig. 48), indicating that TDCOF provides sensing active sites for porous heterojunction materials. Upon the recombination of $(NH_2)_{1.24}$-UiO-66 and TDCOF to form heterojunction, the sensing performance is markedly improved, suggesting that $(NH_2)_{1.24}$-UiO-66 also played a certain role in enhancing the performance of $(NH_2)_{1.24}$-UiO-66@TDCOF. The wavelength-dependent photoconductivity and sensing reveal that $(NH_2)_{1.24}$-UiO-66 influences the efficiency of charge separation within the heterojunction, which in turn impacts its sensing performance. Moreover, UiO-66 with varying numbers of amino groups facilitates energy-level modulation, optimizing charge separation efficiency of the heterojunction, thus further promoting the gas sensing performance of porous heterojunction materials.

To achieve the customization of porous heterojunction with superior reaction efficiency for various chemical applications, the precise regulation of the energy-level in porous heterojunctions is necessary. In this work, porous heterojunction is constructed in a core-shell nanostructure, where the core is $(NH_2)_x$-UiO-66 octahedral nanoparticle, a MOF material and the shell is a layer of TDCOF, a COF material. By the ligand modification in MOF core to achieve precise regulation of energy-level, $(NH_2)_x$-UiO-66@TDCOF porous heterojunction transitions flexibly from a type-I to a type-II configuration, which remarkably enhance the efficiency of charge separation under light irradiation, resulting in excellent chemiresistive gas sensing performances. Notably, the sensitivity of $(NH_2)_{1.24}$-UiO-66@TDCOF toward NO_2 is at a high level among all known heterojunction materials under visible-light condition and leading the field among all reported MOF and COF materials. Moreover, it also shows excellent selectivity to common interference gases and long-term stability for up to 35 days. This work not only introduces a porous heterojunction design but also demonstrates its powerful application in enhancing chemical performance, particularly for gas detection.

Methods

Materials

All solvents and reagents obtained from commercial sources were used without further purification. $ZrCl_4$ (98%) was purchased from Acros Organics. 2,5-Diaminoterephthalic acid ($(NH_2)_2$-H_2BDC, 97%) was purchased from Shanghai Tengqian Biotechnology Co., Ltd. Terephthalic acid (H_2BDC, 98%), 2-aminoterephthalic acid (NH_2-H_2BDC, 99%), 5,10,15,20-tetrakis(4-aminophenyl)porphyrin (TAPP, 98%) and 1,2-dichlorobenzene (AR) were purchased from Shanghai Aladdin. 2,6-Diformylpyridine (DFP, 98%) was purchased from Adamas. Acetic acid

(HAc, 99%), ethanol (EtOH, AR), N,N-dimethylformamide (DMF, AR) and tetrahydrofuran (THF, AR) were purchased from Sinopharm Chemical Reagent Co., Ltd.

Characterization and instruments

Powder X-Ray diffraction (PXRD) patterns of samples were carried out on a Rigaku SmartLab (Japan) equipped with Cu Kα radiation (λ = 1.54060 Å). The element content of samples was determined through an element analyzer (Germany, vario MACRO cube). The scanning electron microscopy (SEM, ZEISS Sigma 500) and transmission electron microscope (TEM, Tecnai F20) were applied to investigate the morphology of the samples. N_2 adsorption tests were measured using a BELSORP MAX automatic volumetric gas adsorption analyzer and samples were pretreated at 200 °C, 24 h. The bandgap of samples was carried out on UV-visible spectrophotometer (Lambad 950). Mott-Schottky measurements were performed on a CHI 660e electrochemical workstation at the frequencies of 500, 1112, and 1658 Hz. The Fourier Transform Infrared (FT-IR) spectra were recorded from KBr pellets in the range 4000–400 cm^{-1} on Nicolet 170 SXFT-IR spectrometer. A xenon arc lamp (PLS-SXE300D) with a light filter (420–760 nm) was utilized as an irradiation source. The photoluminescence spectra (PL) of the samples were recorded in FLS1000 Fluorescence Spectrometer, with an excitation wavelength of 420 nm (test temperature: room temperature; light source: Xenon lamp). The software of date collection (Labview 8.2, OPUS, Cary WinFLR, and XRD Measurement) and date analysis (Origin 2021, BELMaster7, XPSPEAK41, and GMS3)

Synthesis of $(NH_2)_x$-UiO-66

A mixture of $ZrCl_4$ (79 mg, 0.34 mmol) and 2-aminoterephthalic acid (62 mg, 0.34 mmol) was added to 78 mL DMF in a 100 mL flask. Acetic acid (6 mL) was added into the mixture and sonicated for 40 min, forming a clear brown solution. The flask was tightly capped and heated in an oven at 85 °C under static conditions. After 48 h, the product was obtained. The sample was washed with DMF and EtOH each for 3 times. After drying at 85 °C for 48 h, NH_2-UiO-66 was obtained.

The NH_2-UiO-66 with different amounts of amino groups were synthesis based on ligands design to fine-tune the above method. The relevant details can be found in Supplementary Table 1. The content of C and N in these samples was determined through elemental analysis to calculate the average number of amino groups in single ligand of these samples represented by x (Supplementary Table 2). These samples were named $(NH_2)_x$-UiO-66 [$(NH_2)_{0.44}$-UiO-66 | C: N = 2.00: 0.11; $(NH_2)_{0.72}$-UiO-66 | 2.00: 0.18; $(NH_2)_{0.87}$-UiO-66 | 1.94: 0.21; $(NH_2)_{1.00}$-UiO-66 | 2.00: 0.25; $(NH_2)_{1.24}$-UiO-66 | 2.20: 0.34; $(NH_2)_{1.44}$-UiO-66 | 2.27: 0.41; $(NH_2)_{1.69}$-UiO-66 | 2.22: 0.47; $(NH_2)_{2.00}$-UiO-66 | 2.00: 0.50].

Synthesis of TDCOF

The synthesis method of TDCOF followed previously reported procedure[27]. TAPP (27.1 mg, 0.04 mmol), DFP (10.8 mg, 0.08 mmol), EtOH (0.1 mL), 1,2-dichlorobenzene (0.9 mL) and acetic acid (6 M, 0.3 mL) were mixed in a Pyrex tube (o.d × length, 19 × 65 mm and volume, 10 mL). After sonication for about 25 min, the tube was flash-frozen at 77 K (liquid N_2 bath)and degassed to achieve an internal pressure of ~100 mTorr after three freeze-pump-thaw cycles. After the temperature recovered to room temperature, the mixture was heated in an oven at 120 °C for 120 h. After cooling to room temperature, the obtained product was filtrated and transferred to a Soxhlet extractor and washed with THF (24 h). After drying at 120 °C for 24 h, the TDCOF was obtained.

Synthesis of $(NH_2)_x$-UiO-66@TDCOF

$(NH_2)_x$-UiO-66 (20 mg), DFP (10.8 mg, 0.08 mmol), EtOH (0.1 mL), 1,2-dichlorobenzene (0.9 mL) and acetic acid (6 M, 0.3 mL) were mixed in a Pyrex tube (o.d × length, 19 × 65 mm and volume, 10 mL). After sonication for about 40 min, the mixture was heated in an oven at 120 °C for 24 h. After the temperature recovered to room temperature, TAPP (27.1 mg, 0.04 mmol) was added into the mixture. The subsequent treatment was similar to the synthesis of TDCOF. This can be attributed to two factors: (1) the total amount of pendant NH_2 group on the surface of MOF is few, which only consume a very small proportion of DFP amount; and (2) since imide formation is a reversible reaction, the reagents cannot achieve complete conversion. Therefore, the reactants involved in the preparation reaction of $(NH_2)_x$-UiO-66@TDCOF are adequate for synthesizing TDCOF shell. Based on different $(NH_2)_x$-UiO-66, the different $(NH_2)_x$-UiO-66@TDCOF were obtained and named $(NH_2)_{0.44}$-UiO-66@TDCOF, $(NH_2)_{0.72}$-UiO-66@TDCOF, $(NH_2)_{0.87}$-UiO-66@TDCOF, $(NH_2)_{1.00}$-UiO-66@TDCOF, $(NH_2)_{1.24}$-UiO-66@TDCOF, $(NH_2)_{1.44}$-UiO-66@TDCOF, $(NH_2)_{1.69}$-UiO-66@TDCOF, and $(NH_2)_{2.00}$-UiO-66@TDCOF, respectively. In these hybrid materials, the COF loading is ~20.5 wt%.

Gas sensor characterization

Device fabrication. The test sample (10 mg) was dispersed in ethanol by grinding. Then, a quantitative sample (20 μL) is coated on the Ag-Pd interdigital electrode (size: 13.4 × 7 × 0.635 mm^3; electrode spacing: 0.12 mm) using a pipette. Through sticking gold wires on both ends, the sensing test device is fabricated. The photos of device are shown in Supplementary Fig. 1. Further, the *I-V* curves of device at room temperature show linear contours, indicating ohmic contact between the sample and Ag-Pd interdigital electrode (Supplementary Fig. 2).

Gas sensing test. The gas sensor characterization was conducted by a home-made system reported in our previous work[35]. It takes ~0.65 min to fulfill the quartz chamber when the gas flow was 600 mL min^{-1}. The target gas was introduced (3 min) into the quartz tube by mixing the certified gas "mixtures" (Beijing Hua Yuan Gas Chemical Industry Co., Ltd., China) and dry air in a proper ratio controlled by the mass flow controllers (CS-200C, Beijing Sevenstar Qualiflow Electronic Equipment Manufacturing Co., Ltd., China) under visible-light irradiation (λ = 420–760 nm) and room temperature. The constant flow was 600 mL min^{-1}, the bias on the sensor was 5 V and the current was recorded using Keithley 4200 Sourcemeter.

The sensor response with a positive response in this work is defined as the ratio of sensor resistance in the air (R_{air}) and analytic gas ($R_{analyte}$) (Eq. (2)):

$$\text{Response} = R_{air}/R_{analyte} - 1 \quad (2)$$

The sensitivity (*S*) is the ratio of response (*R*) to concentration (*C*) (Eq. (3)):

$$S = R/C \quad (3)$$

The response time ($t_{res.}$) of the sensor with a positive response is the time required for the increasing current to 90% of the saturation value and the recovery time ($t_{rec.}$) is the time required to decrease the saturated current to its 10%.

The coefficient of variation (CV) is used to represent the change of different cycles on responses, which is defined as (Eq. (4)):

$$CV = R_{SD}/R_{average} \times 100\% \quad (4)$$

R_{SD} and $R_{average}$ are the standard deviation (SD) and an average value of responses with different cycles (100 ppm NO_2), respectively.

To ensure the accuracy of the results, all tests were conducted 3–5 time using the materials obtained from at least three different batches of synthesis. Taking $(NH_2)_{1.24}$-UiO-66@TDCOF for example, the results are showed in Supplementary Table 3.

Reporting summary

Further information on research design is available in the Nature Portfolio Reporting Summary linked to this article.

Data availability

All relevant data that support the findings of this study are presented in the manuscript and supplementary information file. Raw data can be obtained from the corresponding author upon request. Source data are provided with this paper.

References

1. Zhu, B., Sun, J., Zhao, Y., Zhang, L. & Yu, J. Construction of 2D S-scheme heterojunction photocatalyst. *Adv. Mater.* **36**, e2310600 (2024).
2. Dhakshinamoorthy, A., Li, Z., Yang, S. & Garcia, H. Metal-organic framework heterojunctions for photocatalysis. *Chem. Soc. Rev.* **53**, 3002–3035 (2024).
3. Zu, D. et al. Oxygen vacancies trigger rapid charge transport channels at the engineered interface of s-scheme heterojunction for boosting photocatalytic performance. *Angew. Chem. Int. Ed.* e202405756 (2024).
4. Li, X. et al. Constructing heterojunctions by surface sulfidation for efficient inverted perovskite solar cells. *Science* **375**, 434–437 (2022).
5. Sulas-Kern, D. B., Miller, E. M. & Blackburn, J. L. Photoinduced charge transfer in transition metal dichalcogenide heterojunctions-towards next generation energy technologies. *Energy Environ. Sci.* **13**, 2684–2740 (2020).
6. Niu, Y. et al. A photovoltaic self-powered gas sensor based on all-dry transferred MoS_2/GaSe heterojunction for ppb-level NO_2 sensing at room temperature. *Adv. Sci.* **8**, e2100472 (2021).
7. Xu, F. et al. Unique S-scheme heterojunctions in self-assembled TiO_2/$CsPbBr_3$ hybrids for CO_2 photoreduction. *Nat. Commun.* **11**, 4613 (2020).
8. Rahman, E. et al. Controlling the selectivity of chlorine evolution reaction by $IrTaO_x$/TiO_2 heterojunction anodes: mechanism and real wastewater treatment. *ACS Catal.* **14**, 8427–8436 (2024).
9. Rogalski, A. Detectivities of WS_2/HfS_2 heterojunctions. *Nat. Nanotechnol.* **17**, 217–219 (2022).
10. Zhang, M. et al. An irradiance-adaptable near-infrared vertical heterojunction phototransistor. *Adv. Mater.* **34**, e2205679 (2022).
11. Sarango-Ramirez, M. K. et al. Void space versus surface functionalization for proton conduction in metal-organic frameworks. *Angew. Chem. Int. Ed.* **60**, 20173–20177 (2021).
12. Su, A. Y., Apostol, P., Wang, J., Vlad, A. & Dinca, M. Electrochemical capacitance traces with interlayer spacing in two-dimensional conductive metal-organic frameworks. *Angew. Chem. Int. Ed.* **63**, e202402526 (2024).
13. Heinke, L. & Woll, C. Surface-mounted metal-organic frameworks: crystalline and porous molecular assemblies for fundamental insights and advanced applications. *Adv. Mater.* **31**, e1806324 (2019).
14. Yu, T. Y. et al. Interpenetrating 3D covalent organic framework for selective stilbene photoisomerization and photocyclization. *J. Am. Chem. Soc.* **145**, 8860–8870 (2023).
15. Feng, B. et al. Isomeric dual-pore two-dimensional covalent organic frameworks. *J. Am. Chem. Soc.* **145**, 26871–26882 (2023).
16. Zhang, X., Geng, K., Jiang, D. & Scholes, G. D. Exciton diffusion and annihilation in an sp2 carbon-conjugated covalent organic framework. *J. Am. Chem. Soc.* **144**, 16423–16432 (2022).
17. Wang, B. et al. Microporous hydrogen-bonded organic framework for highly efficient turn-up fluorescent sensing of aniline. *J. Am. Chem. Soc.* **142**, 12478–12485 (2020).
18. Gao, J. et al. A microporous hydrogen-bonded organic framework for the efficient capture and purification of propylene. *Angew. Chem. Int. Ed.* **60**, 20400–20406 (2021).
19. Lin, R. B. et al. Molecular sieving of ethylene from ethane using a rigid metal-organic framework. *Nat. Mater.* **17**, 1128–1133 (2018).
20. Wu, C. et al. Enhancing the gas separation selectivity of mixed-matrix membranes using a dual-interfacial engineering approach. *J. Am. Chem. Soc.* **142**, 18503–18512 (2020).
21. Yang, Y. L. et al. A honeycomb-like porous crystalline hetero-electrocatalyst for efficient electrocatalytic CO_2 reduction. *Adv. Mater.* **34**, e2206706 (2022).
22. Prominski, A. et al. Porosity-based heterojunctions enable leadless optoelectronic modulation of tissues. *Nat. Mater.* **21**, 647–655 (2022).
23. Xie, D. et al. Porous metal-organic framework/ReS_2 heterojunction phototransistor for polarization-sensitive visual adaptation emulation. *Adv. Mater.* **35**, e2212118 (2023).
24. Cho, S. et al. Interface-sensitized chemiresistor: integrated conductive and porous metal-organic frameworks. *Chem. Eng. J.* **449**, 137780 (2022).
25. Le Huec, T. et al. Heteroepitaxial MOF-on-MOF photocatalyst for solar-driven water splitting. *ACS Nano* **18**, 20201–20212 (2024).
26. Tan, K. et al. Defect termination in the UiO-66 family of metal–organic frameworks: the role of water and modulator. *J. Am. Chem. Soc.* **143**, 6328–6332 (2021).
27. Chen, Y. J. et al. Dangling bond formation on COF nanosheets for enhancing sensing performances. *Chem. Sci.* **14**, 4824–4831 (2023).
28. Zhang, M. et al. Semiconductor/covalent-organic-framework Z-scheme heterojunctions for artificial photosynthesis. *Angew. Chem. Int. Ed.* **59**, 6500–6506 (2020).
29. Chen, Y. J. et al. TiO_2@COF nanowire arrays: a "Filter Amplifier" heterojunction strategy to reverse the redox nature. *Nano Lett.* **23**, 3614–3622 (2023).
30. Zhang, M. et al. Controllable synthesis of COFs-based multi-component nanocomposites from core-shell to yolk-shell and hollow-sphere structure for artificial photosynthesis. *Adv. Mater.* **33**, e2105002 (2021).
31. Lu, M. et al. Confining and highly dispersing single polyoxometalate clusters in covalent organic frameworks by covalent linkages for CO_2 photoreduction. *J. Am. Chem. Soc.* **144**, 1861–1871 (2022).
32. Low, J., Dai, B., Tong, T., Jiang, C. & Yu, J. In situ irradiated X-ray photoelectron spectroscopy investigation on a direct Z-scheme TiO_2/CdS composite film photocatalyst. *Adv. Mater.* **31**, 1802981 (2019).
33. Xu, Q., Zhang, L., Cheng, B., Fan, J. & Yu, J. S-scheme heterojunction photocatalyst. *Chem* **6**, 1543–1559 (2020).
34. Ma, K. et al. Holistic energy landscape management in 2D/3D heterojunction via molecular engineering for efficient perovskite solar cells. *Sci. Adv.* **9**, eadg0032 (2023).
35. Yao, M. S., Tang, W. X., Wang, G. E., Nath, B. & Xu, G. MOF thin film-coated metal oxide nanowire array: significantly improved chemiresistor sensor performance. *Adv. Mater.* **28**, 5229–5234 (2016).
36. Eom, T. H. et al. Substantially improved room temperature NO_2 sensing in 2-dimensional SnS_2 nanoflowers enabled by visible light illumination. *J. Mater. Chem. A* **9**, 11168–11178 (2021).
37. Cho, D. et al. Optically activated 3D thin-shell TiO_2 for super-sensitive chemoresistive responses: toward visible light activation. *Adv. Sci.* **8**, 2001883 (2021).
38. Hoffmann, M. W. et al. Highly selective SAM–nanowire hybrid NO_2 sensor: insight into charge transfer dynamics and alignment of frontier molecular orbitals. *Adv. Funct. Mater.* **24**, 595–602 (2014).

39. Lim, K. et al. A transparent nanopatterned chemiresistor: visible-light plasmonic sensor for trace-level NO_2 detection at room temperature. *Small* **17**, 2100438 (2021).
40. Han, S. et al. Visible-photoactive perovskite ferroelectric-driven self-powered gas detection. *J. Am. Chem. Soc.* **145**, 12853–12860 (2023).
41. Vijjapu, M. T. et al. Fully integrated indium gallium zinc oxide NO_2 gas detector. *ACS Sens.* **5**, 984–993 (2020).
42. Wang, X.-X., Li, H.-Y. & Guo, X. Flexible and transparent sensors for ultra-low NO_2 detection at room temperature under visible light illumination. *J. Mater. Chem. A* **8**, 14482–14490 (2020).
43. Geng, X. et al. Photoexcited NO_2 enables accelerated response and recovery kinetics in light-activated NO_2 gas sensing. *ACS Sens.* **6**, 4389–4397 (2021).
44. Li, Y. et al. Preparation of BiOI-functionalized ZnO nanorods for Ppb-level NO_2 detection at room temperature. *ACS Sens.* **7**, 3915–3922 (2022).
45. Wang, T. et al. Bifunctional gas sensor based on Bi_2S_3/SnS_2 heterostructures with improved selectivity through visible light modulation. *J. Mater. Chem. A* **10**, 4306–4315 (2022).
46. Jo, Y.-M. et al. Visible-light-activated type II heterojunction in Cu_3(hexahydroxytriphenylene)$_2/Fe_2O_3$ hybrids for reversible NO_2 sensing: critical role of π–π* transition. *ACS Cent. Sci.* **7**, 1176–1182 (2021).
47. Choi, J., Kim, T., Li, H., Jung, H. T. & Zhao, D. Gas sensors with two-dimensional rGO@COF composite materials for fast NO_2 detection under room temperature. *ACS Appl. Mater. Interfaces* **15**, 44119–44126 (2023).
48. Kim, J. O. et al. Large-area synthesis of nanoscopic catalyst-decorated conductive MOF film using microfluidic-based solution shearing. *Nat. Commun.* **12**, 4294 (2021).
49. ME, D. M., Sundaram, N. G., Singh, A., Singh, A. K. & Kalidindi, S. B. An amine functionalized zirconium metal-organic framework as an effective chemiresistive sensor for acidic gases. *Chem. Commun.* **55**, 349–352 (2019).
50. Meng, Z., Stolz, R. M. & Mirica, K. A. Two-dimensional chemiresistive covalent organic framework with high intrinsic conductivity. *J. Am. Chem. Soc.* **141**, 11929–11937 (2019).
51. Wang, J. et al. Moisture-insensitive and highly selective detection of NO_2 by ion-in-conjugation covalent organic frameworks. *ACS Sens.* **7**, 3782–3789 (2022).
52. Weber, I. C., Braun, H. P., Krumeich, F., Guntner, A. T. & Pratsinis, S. E. Superior acetone selectivity in gas mixtures by catalyst-filtered chemoresistive sensors. *Adv. Sci.* **7**, 2001503 (2020).
53. Yang, L. et al. Quasi similar routes of NO_2 and NO sensing by nanocrystalline WO_3: evidence by in situ DRIFT spectroscopy. *Sensors* **19**, 3405 (2019).
54. Peterson, G. W., Mahle, J. J., DeCoste, J. B., Gordon, W. O. & Rossin, J. A. Extraordinary NO_2 removal by the metal-organic framework UiO-66-NH_2. *Angew. Chem. Int. Ed.* **55**, 6235–6238 (2016).
55. Li, D., Chen, W., Wu, J., Jia, C. Q. & Jiang, X. The preparation of waste biomass-derived N-doped carbons and their application in acid gas removal: focus on N functional groups. *J. Mater. Chem. A* **8**, 24977–24995 (2020).

Acknowledgements

This work was financially supported by the Project Funded by China Postdoctoral Science Foundation (CPSF) under grant number of 2023M743496 (Y.-J.C.), the Postdoctoral Fellowship Program of CPSF under grant number of GZC20241722 (Y.-J.C.), National Natural Science Foundation of China (22325109 (G.X.), 91961115, (G.X.) 22171263 (G.X.), 22405274 (J.-F.L.), and 62227815 (G.X.)), Scientific Research and Equipment Development Project of CAS (YJKYQ20210024 (G.X.)), Fujian Science & Technology Innovation Laboratory for Optoelectronic Information of China (2021ZR101 (G.X.)), the Natural Science Foundation of Fujian Province (2021J02017 (G.X.)) and Self-deployment Project Research Program of Haixi Institutes, Chinese Academy of Sciences (CXZX-2022-GH09 (G.X.)).

Author contributions

Y.-J.C. and G.X. conceived the idea. Y.-J.C., X.-L.Y., Z.-P.L. and S.-P. Z. designed the experiments, collected and analyzed the data. Y.-M.X. accomplished the theoretical calculation. K.-F.L., J.-F.L., and G.-E.W. assisted with the experiments and characterizations. Y.-J.C. and G.X. wrote the manuscript. All authors discussed the results and commented on the manuscript.

Competing interests

The authors declare no competing interests.

Additional information

Supplementary information The online version contains supplementary material available at https://doi.org/10.1038/s41467-025-61836-5.

Correspondence and requests for materials should be addressed to Gang Xu.

Peer review information *Nature Communications* thanks Yeong Don Park and Hoi Ri Moon for their contribution to the peer review of this work. A peer review file is available.